*Article*

# Interfacial Electronic Rearrangement and Synergistic Catalysis for Alkaline Water Splitting in Carbon-Encapsulated Ni (111)/Ni₃C (113) Heterostructures

**Xiaoyu Li [1,†], Zhenbo Peng [2,†], Dongmei Jia [1,†], Yikang Wang [1], Wenbo Wu [1], Ping Deng [1], Mengqiu Xu [1], Xudong Xu [1], Gan Jia [1,\*], Wei Ye [1,\*] and Peng Gao [1,\*]**

[1] College of Material, Chemistry and Chemical Engineering, Hangzhou Normal University, Hangzhou 311121, China
[2] Zhejiang Collaborative Innovation Center for High Value Utilization of Byproducts from Ethylene Project, Ningbo Polytechnic, Ningbo 315800, China
\* Correspondence: gjia@hznu.edu.cn (G.J.); yewei@hznu.edu.cn (W.Y.); gaopeng@hznu.edu.cn (P.G.)
† These authors contributed equally to this work.

**Abstract:** The realization of efficient water electrolysis is still blocked by the requirement for a high and stable driving potential above thermodynamic requirements. An Ni-based electrocatalyst, is a promising alternative for noble-metal-free electrocatalysts but tuning its surface electronic structure and exposing more active sites are the critical challenges to improving its intrinsic catalytic activity. Here, we tackle the challenge by tuning surface electronic structures synergistically with interfacial chemistry and crystal facet engineering, successfully designing and synthesizing the carbon-encapsulated Ni (111)/Ni₃C (113) heterojunction electrocatalyst, demonstrating superior hydrogen evolution reaction (HER) activities, good stabilities with a small overpotential of −29 mV at 10 mA/cm$^2$, and a low Tafel slope of 59.96 mV/dec in alkaline surroundings, approximating a commercial Pt/C catalyst and outperforming other reported Ni-based catalysts. The heterostructure electrocatalyst operates at 1.55 V and 1.26 V to reach 10 and 1 mA cm$^{-2}$ in two-electrode measurements for overall alkaline water splitting, corresponding to 79% and 98% electricity-to-fuel conversion efficiency with respect to the lower heating value of hydrogen.

**Keywords:** electrocatalyst; nickel-based materials; interfacial electronic rearrangement; overall water splitting

## 1. Introduction

As a clean and renewable energy, hydrogen has been widely admitted as a substitute for decreasing fossil fuel. A hydrogen evolution reaction (HER) in electrocatalytic overall water splitting (OWS) is widely admitted as a practical and appealing route to produce high purity hydrogen [1]. Unfortunately, the large kinetic barrier and slow kinetics of OWS usually leads to higher overpotentials [2], which determines that an efficient OWS electrocatalyst should be used to reduce the associated energy losses. By now, noble metal-based catalysts are still the most active and stable ones for it, although their high cost and scarcity greatly block their large-scale water splitting utilization. Thus, scientists show solicitude for developing different sorts of cost-effective and sustainable alternatives, such as non-precious metal, transition metal hydroxides [3,4], transition metal oxides [5–7], transition metal sulfides [8,9], transition metal carbides [10,11], and metal phosphides [12,13].

Routinely, the mechanism of alkaline HER in OWS consists of a water dissociation step through breaking the HO-H bond (Volmer step), followed by H₂ generation (Heyrovsky step or Tafel step) [14]. According to the "volcanic effect" curve, transition metals, such as Ni, Co, Mo, and Fe, have higher current density and lower overpotential due to their unoccupied d orbitals and unpaired d electrons [15–20]. However, the reported volcano

plots for HER kinetics as a function of M-H bond energies generally do not consider actual acidity and alkalinity in the atmosphere. For example, the Volmer step in alkaline conditions not only depends on the adsorption energy of hydrogen but is also related to the adsorption energy of water and the desorption energy of the hydroxide anion. Low water adsorption energy can lead to insufficient reactants, whereas high hydroxide anion adsorption energy causes a poisoning effect because of a loss of catalytically active sites. Therefore, their activities towards the OWS needs to be improved through tuning their electronic structures and exposing more active sites to cater to the above needs. Until now, no single non-precious metal has been proven to possess the suitable electronic structures needed to meet the above conditions by itself, although their selected crystal plane with the lowest surface energy were presented, as (111) with fcc Ni or (001) for hcp Co, Zn, and Cd [21]. Naturally, many researchers turn their attention to exploring new strategies to tune the catalyst's surface electronic structure and active sites to elevate their electrocatalytic activities, such as surface engineering, doping, single-atom anchoring, phase structures, and defects. Nevertheless, most strategies inevitably decrease the metal's electronic transport capacity and phase stability. To solve these puzzles, the OWS activity of a pure metal phase could be improved by constructing a robust heterogeneous boundary, in which the electronic structure of metal electrocatalyst is optimized and new complementary active sites are simultaneously introduced without matrix changing. This is also more practical and feasible for large-scale industrial production.

Metal nickel is well-known as an HER catalyst and persistent efforts have been undertaken to ameliorate Ni-based catalysts as alkaline electrolysers. Therefore, it is expected to be able to further enhance its HER performance and stability via electrode design, Recently, more efforts have been undertaken to optimize the chemical structures and morphology of Ni-based heterojunction catalysts, which display promising HER or/and oxygen evolution reaction (OER) catalytic activity for an efficient water splitting process. For example, Xiong et al. developed a novel core-shell nanorod array for pH-universal HER application, in which an amorphous $Rh(OH)_3$ shell provided rich active sites promoting reactants and the crystalline NiTe nanorod core enhanced conductivity [22]. The activity of $Ni(OH)_2$/Ni structures is increased by about four times compared to nanostructured Ni, in which $Ni(OH)_2$ not only promotes $H_2O$ dissociation, but also stabilizes the $H_2O$-surrounded cations [23]. A similar mechanism has also been realized in an NiO/Ni heterojunction where a 10 mA $cm^{-2}$ at <100 mV overpotential was achieved [24]. An obvious decay in current density was observed, suggesting the instability of the NiO-Ni nanostructures under HER operation conditions, which came from the obvious oxidation of the Ni core and phase separation between NiO and Ni [25]. All the above works indicate that a direct exposure to the alkaline environment of metal Ni and Ni-based compounds inevitably brought about unsatisfactory catalytic stability due to alkaline corrosion, which urgently needs a protective mechanism, such as new complementary active sites and carbon protection. In summary, although the heterojunction-phase catalyst further improves HER and OER activity, the construction of a highly stable heterostructure and the understanding and regulation of its surface electronic structure and active sites on the interface are still huge challenges.

Recently, DFT calculations certify that coupling Ni with $Ni_3C$ can rearrange their electronic structures and optimize the adsorption energies of OER intermediates, hydrogen and water molecules [26]. Therefore, experimentally, we try to tune metal Ni electronic structure through a Ni-$Ni_3C$ heteroconjunction synergistic with nitrogen contained carbon (NC) protection, and then successfully design and prepare a series of high-density heterojunction-interface electrocatalysts (denoted Ni-$Ni_3C$/NC) with outstanding HER, OER, and OWS activities and stabilities in alkaline surroundings. Starting from a hydrothermally synthesized Ni-NTA (nitrilotriacetic acid) precursor, we develop a simple surface electronic structure modulation strategy of constructing NC-coated multi-heterogeneous-phase interface Ni (111)-$Ni_3C$ (113)/NC electrocatalysts (Scheme 1) by a secondly controlled thermal decomposition. Our approach can realize not only the rearrangement of electronic

structures and new complementary active sites, but also mesoporous NC protection. Additionally, the as-prepared Ni-Ni$_3$C/NC multi-heterogeneous catalyst exhibits remarkable HER catalytic activity, achieving low overpotentials of $-29$ mV for HER at a current density of 10 mA/cm$^2$. They also have a Tafel slope of 59.96 mV/dec in 1.0 M KOH media, and good stability during testing for 100 h in the media. The catalysts showed superior activities with Tafel slope values and overpotentials lower than the values reported for Ni-base HER catalysts in alkaline media [27–29]. More importantly, the as-synthesized Ni-Ni$_3$C/NC catalyst also exhibits excellent OER and OWS catalytic activity. In OWS, the material system operates at 1.55 V and 1.26 V to reach 10 and 1 mA cm$^{-2}$ in two-electrode measurements, corresponding to 79% and 98% electricity-to-fuel conversion efficiency with respect to the lower heating value of hydrogen. DFT calculation results further confirm that the heterojunction between Ni (111) and Ni$_3$C (113) can regulate their electronic structure effectively for lowering the Gibbs free energy of H$_2$O dissociation. The in-situ Raman spectra and FT-IR spectra indicate that the presence of Ni$_3$C has the function to inhibit Ni self-oxidation and promote water dissociation into H$_2$ in the hydrogen evolution reaction (HER) process by the formed OH$_{ad}$-Ni$^{2+}$ and H$_{ad}$-Ni$^0$ species, whereas OH$^-_{ad}$-Ni$^{3+}$ and H$_{ad}$-Ni$^0$ were created during the oxygen evolution reaction (OER). This work provides an easy-to-accomplish engineering strategy for nonprecious metal-based heterostructures with excellent and stable electrocatalytic activity.
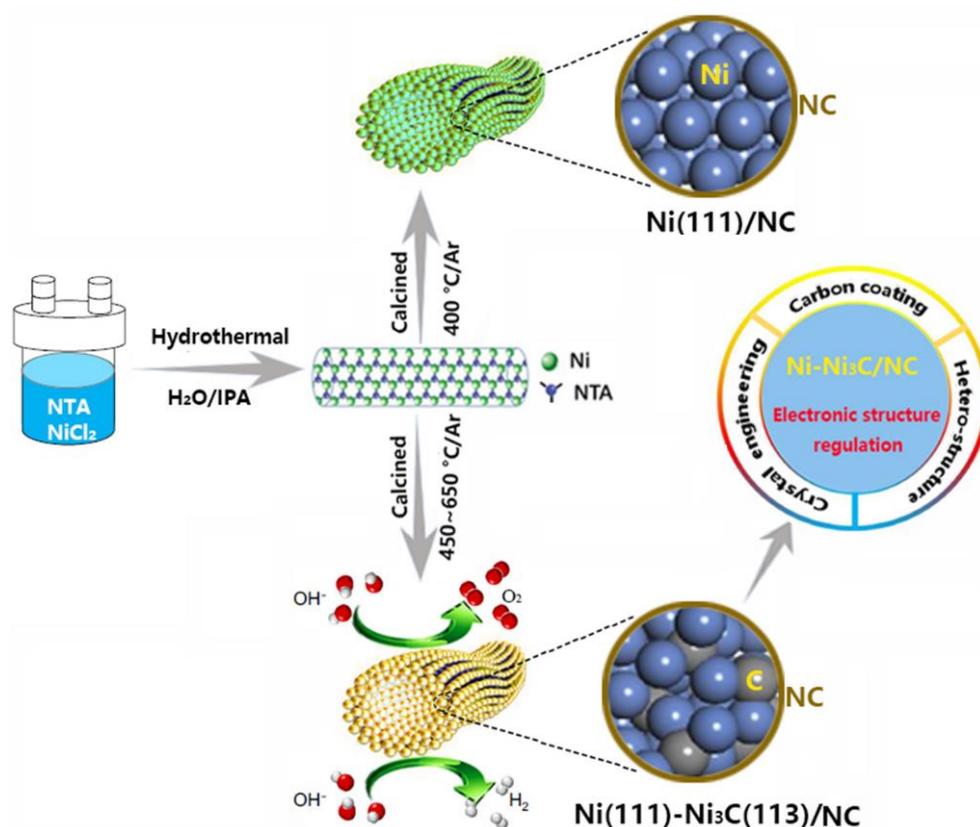


**Scheme 1.** A surface electronic structure modulation strategy of constructing multi-heterogeneous-phase interface Ni-Ni$_3$C/NC electrocatalysts.

## 2. Results

### 2.1. Structural and Composition Characterization of Ni-Ni$_3$C/NC

Firstly, as shown in Figure S1 (ESI†), nanorod-like Ni-NTA samples with a smooth surface have been obtained and the corresponding measurement results agree well with our previous work [30], which confirms that the linear polymerization between NTA molecules had been formed, leading to the one-dimensional structure of the Ni-NTA product. After carefully controlled calcination at different temperatures by us, rhombohedral

$Ni_3C$ and crystalline carbon were formed beside metal Ni (Figure 1a) once the temperature was reached 450 °C, which was analyzed by X-ray diffraction (XRD) measurements. The samples calcined at 400, 450, 500, 550, and 600 °C are named as $Ni-Ni_3C/NC-400$, $Ni-Ni_3C/NC-450$, $Ni-Ni_3C/NC-500$, $Ni-Ni_3C/NC-550$, and $Ni-Ni_3C/NC-600$, respectively. As shown in Figure 1a, the diffraction peaks coincided well with the rhombohedral $Ni_3C$ (JCPDS No. 72-1467), cubic Ni (JCPDS No. 87-0712), and crystalline carbon (JCPDS No. 50-1084). Then, field emission scanning electron microscopy (FESEM) and transmission electron microscopy (TEM) characterizations were implemented to gather morphology information of the as-prepared $Ni-Ni_3C/NC-500$ sample, because it was proven to show the best activity in the following electrocatalytic measurements.
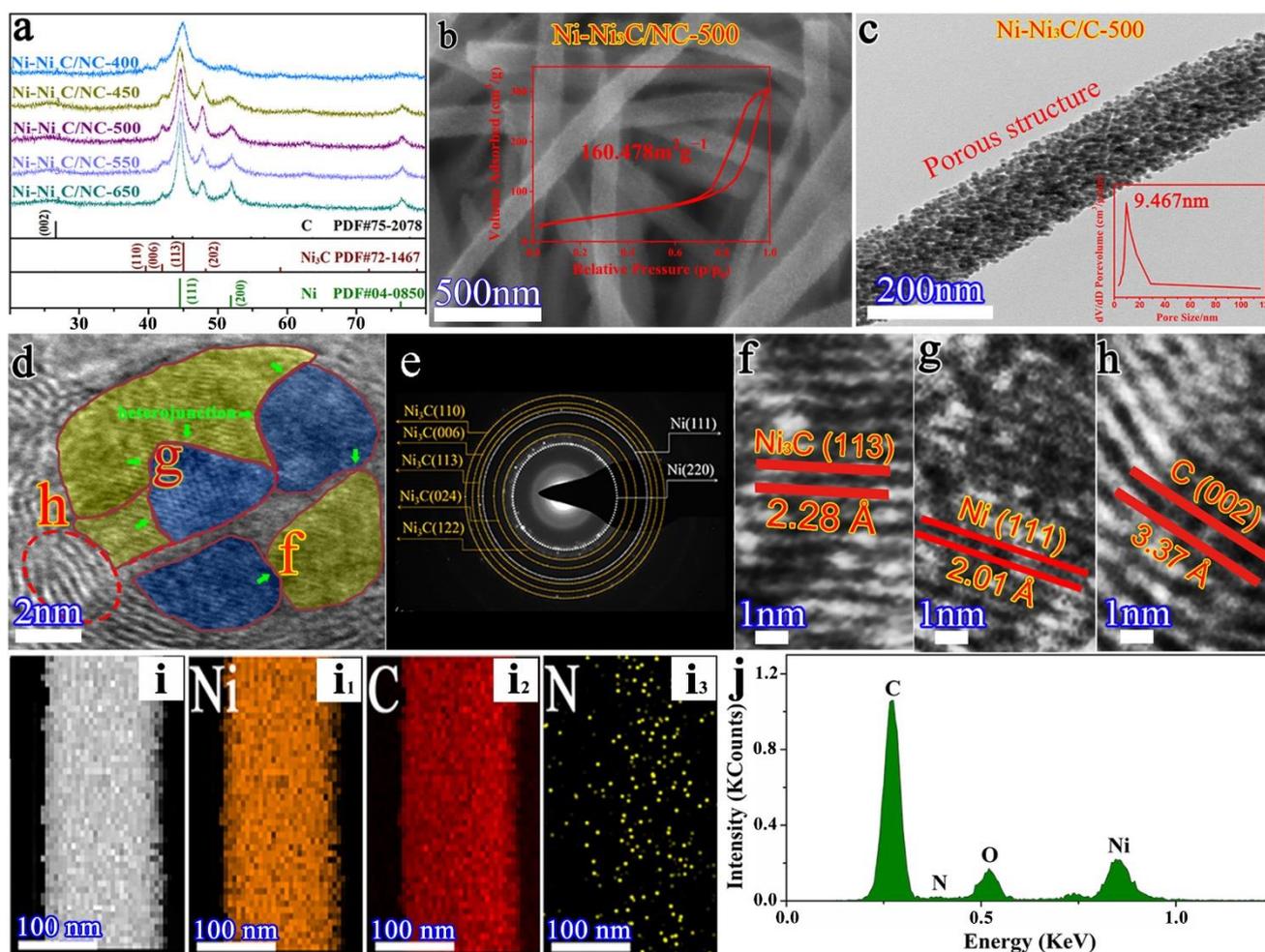


**Figure 1.** Microstructure and composition characterizations of the samples prepared under different thermal decomposition temperatures (400–650 °C). The $Ni-Ni_3C/NC-500$ sample had the best activity in the following electrocatalytic measurements. (**a**) XRD patterns of various as-prepared $Ni-Ni_3C/NC$ samples. (**b,c**) SEM and TEM images of $Ni-Ni_3C/NC-500$. Insets are its $N_2$ adsorption-desorption isotherm and pore-size distribution curve, respectively. (**d–h**) HRTEM and SAED images of $Ni-Ni_3C/NC-500$. (**d**) shows $Ni-Ni_3C/NC-500$ composition distribution (yellow section: $Ni_3C$, blue section: metal Ni) and heterojunction interface. (**e**) shows the heterostructure's lattice fringes. (**f–h**) show $Ni_3C$, Ni, and C lattices. (**i,j**) EDX elemental mappings and EDS spectrum of $Ni-Ni_3C/NC-500$. Scale bars are 100 nm.

As shown in Figure 1b, Figures S2 and S3 (ESI†), $Ni-Ni_3C/NC$ samples calcined at 400–550 °C can still maintain a uniform nanorod shape. However, when the calcination temperature exceeds 550 °C, the nanorods begin to crack. Interestingly, nanorods are

composed of many spherical nanoparticles (~10 nm). These nanoparticles accumulate and exhibit good mesoporous properties, which will surely enhance the molecular/ion diffusion in the catalyst and provide more catalytic active sites [31]. These mesopores are further characterized by $N_2$ adsorption-desorption analysis (Insets in Figure 1b,c; Figure S4, ESI†), which provides their Brunauer-Emmett-Teller (BET) surface areas, which in this case ranged from 143 to 160 $m^2$/g with a same 9.5 nm mesopore size, as summarized in Table S1 (ESI†). According to the IUPAC classification, all the Ni-Ni$_3$C/NC samples show type III isotherms with minimal hysteresis curves, indicating the formation of external macropores [32,33]. The pore sizes of the samples obtained under different calcination temperatures are similar. However, their specific surface area display certain differences [34,35], which may be due to their different aggregation degree of nanospheres induced by distinct nucleation rates under different calcination temperatures. The mesopore size indicated in BET measurements matches well with the diameter of the hollow carbon shell (~10 nm) (Figure 1d). In addition, the Ni-Ni$_3$C/NC-500 sample displays the largest BET surface area, which implies that it could act as an excellent reaction platform with abundant heterogeneous interfaces and active sites conducive to mass transfer. In order to have a clear understanding of the microstructure and composition of the sample, we carried out high-resolution TEM (HRTEM) analysis. As shown in Figure 1d, the high-resolution TEM (HRTEM) images of a presentative Ni-Ni$_3$C/NC-500 nanosphere clearly show multi-hybrid interfaces between Ni$_3$C and metal Ni, suggesting the formation of a tight Ni/Ni$_3$C heterostructure. The formation of the hybrid catalyst mainly pertains to the simultaneous occurrence of agglomeration and atomization under high temperature carbonization. The polycrystalline nature of each nanosphere is also confirmed by the corresponding SAED, as presented in Figure 1e. Their microstructures are further studied by HRTEM measurements, as shown in Figure 1f–h. The well-resolved lattice fringes with inter-planar distances of 0.228 and 0.201 nm can be unambiguously assigned to the (113) crystal planes of Ni$_3$C and the (111) crystal planes of cubic Ni, respectively. Moreover, it is depicted that the carbon frameworks are composed of a ~9 layered (002) plane of graphite with an inter-planar spacing of 0.337 nm. The EDX elemental mapping images (Figure 1i) display the uniform distribution of massive elemental C and Ni across the entire nanorod, illustrating the coupling characteristics of Ni and Ni$_3$C. Sprinkled elemental N is also exposed. The above elemental information agrees with its energy-dispersive X-ray spectroscopy (EDS) characterization (Figure 1j).

Then, we performed an X-ray photoelectron spectroscopy (XPS) measurement to assess the elemental valence states of the as-synthesized Ni-Ni$_3$C/NC-450, Ni-Ni$_3$C/NC-500, and Ni-Ni$_3$C/NC-550 samples due to their hybrid compositions and integrated structures. Their full XPS spectra (Figure S5, ESI†) showed similar atomic ratios of C, N, and Ni, and that the ratio of Ni-Ni$_3$C/NC-500 is equal to 87.46%, 6.37%, and 6.17%, respectively. Their high-resolution spectra of Ni $2P_{3/2}$ are shown in Figure 2a,b, in which, interestingly, two obvious binding energies of $Ni^0$ $2p_{3/2}$ are detected at 851.9 and 852.9 eV. the latter peak located at the normal position of $Ni^0$ $2p_{3/2}$ in metal Ni, which belongs to the ones buried in the internal, and the former should be the $Ni^0$ atoms on the heterostructure interface [36]. Their area ratios are about 0.52:1, 0.65:1, and 0.45:1, which means that Ni-Ni$_3$C/NC-500 has the highest density $Ni^0$ atoms on the heterostructure interface and it is about 1.25 and 1.44 times that of the other two samples. At the same time, the binding energy of $Ni^{2+}$ shifts to a higher position (856.2 eV) compared with the literature of $Ni^{2+}$ in Ni$_3$C (855.4 eV) [37], indicating the interfacial electronic rearrangement in the Ni (111)/Ni$_3$C (113) heterostructure. At the same time, as shown in Figure 2c, the deconvoluted core-level C 1s XPS spectrum reveals the characteristic peak of C-Ni bonds at 284.0 eV, verifying the formation of Ni$_3$C [38,39]. A small amount of N element introduced by the Ni-NTA precursor (Figure 2d) is also observed at 398.8 and 399.8 eV, which is ascribed to pyridinic N and pyrrolic N, respectively.
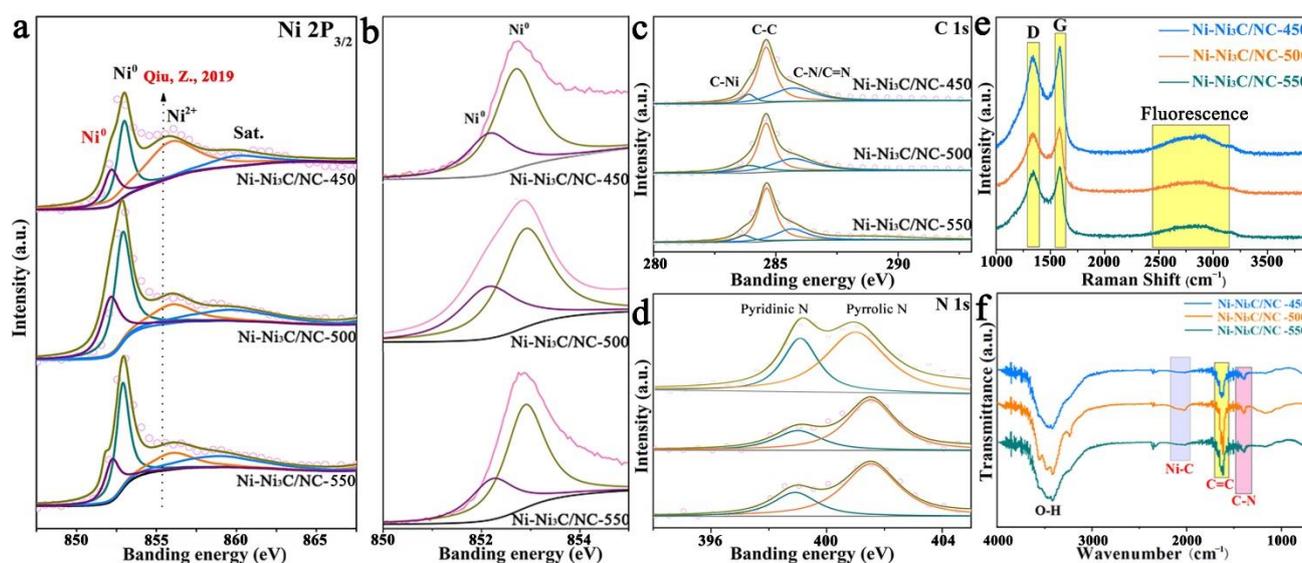
**Figure 2.** Chemical state characterizations of the as-obtained samples. (**a**–**d**) XPS spectra of Ni-Ni$_3$C/NC prepared at 450, 500, and 550 °C. (**a**) Ni 2p spectra, (**b**) enlarged Ni$^0$ 2p spectra. (**c**) C 1s spectra. (**d**) N 1s spectra. (**e**,**f**) Raman and FT-IR spectra of the samples.

It has been proven that N doping in carbon can improve its conductivity by optimizing the electronic structure [40–42], which often exists in pyridine N and pyrrole N form. Comparatively, pyridine N is more conducive to enhance the conductivity of a carbon skeleton [43,44]. Therefore, the nitrogen in Ni-Ni$_3$C/NC, as confirmed by our XPS measurements, can further improve the overall conductivity. Furthermore, three samples' chemical states are characterized by their Raman spectra in a 200~3800 cm$^{-1}$ range (Figure 2e), where only D band (1332 cm$^{-1}$), G band (1587 cm$^{-1}$), and a broad fluorescence peak (2828 cm$^{-1}$) of NC shell are found, with an absence of Ni-based oxides, such as Ni(OH)$_2$, NiO, and NiOOH, which have obvious Raman peaks at 400–560 cm$^{-1}$ [45–51]. The FT-IR spectra of the Ni-Ni$_3$C/NC samples in the range of 700 to 4000 cm$^{-1}$ were recorded, as shown in Figure 2f. In addition to the C-N and C=C signals belonging to CN in the range of 1300 cm$^{-1}$-1635 cm$^{-1}$ and C-H of CN shell at 3430 cm$^{-1}$, an obvious absorption at about 2050 cm$^{-1}$ is also detected, which is ascribed to the conjugated $\nu_{CN}$ bands of Ni-C in Ni$_3$C [52]. All the above results confirm that an interfacial electronic rearrangement in the Ni (111)/Ni$_3$C (113) heterostructure is really performed.

### 2.2. Electrochemical HER of Ni-Ni$_3$C/NC

The alkaline HER activities of the as-obtained Ni-Ni$_3$C/NC samples were investigated in 1 M KOH solution, as shown in Figure S6 (ESI†). In the HER measurements (Figure 3a), Ni-Ni$_3$C/NC-500 has an amazingly low overpotential of −29 mV at a current density of 10 mA cm$^{-2}$, nearly comparable to that of Pt/C. Ni-Ni$_3$C/NC-400, Ni-Ni$_3$C/NC-450, Ni-Ni$_3$C/NC-550, and Ni-Ni$_3$C/NC-650 also exhibit low overpotentials of 133, 41, 66, and 128 mV, respectively. Similar to the above overpotential trend, the resulting Tafel slope of Ni-Ni$_3$C/NC-500 (Figure 3b) has a minimum value of 59.96 mV dec$^{-1}$, which is much less than other Ni-Ni$_3$C/NC samples (82.76~159.34 mV dec$^{-1}$). In alkaline media, the HER on the surface of metal (M) or metal composites contains two primary steps, involving an electron transfer process that forms the adsorbed hydrogen, (H$_2$O + M + e$^-$ ↔ M-H$_{ad}$ + OH$^-$, Volmer reaction) along with an electrochemical desorption process (H$_2$O + M-H$_{ad}$ +e$^-$ ↔ M + H$_2$ + OH$^-$, Heyrovsky reaction) or a chemical desorption process (2M-H$_{ad}$ ↔ 2M + H$_2$, Tafel reaction). According to the HER kinetic model [53], the Tafel slope of 59.96 mV dec$^{-1}$ on the surface of Ni-Ni$_3$C/NC-500 is between the theoretical values for the rate-determining Volmer (120 mV dec$^{-1}$) and Heyrovsky (40 mV dec dec$^{-1}$) cases and thus indicates that the HER is proceeding via a

Volmer-Heyrovsky reaction. According to the Tafel equation, the samples' HER intrinsic activities are depicted in Figure 3c by the exchange current densities ($j_0$). Obviously, Ni-Ni$_3$C/NC-500 exhibits a maximum $j_0$ value of 4.13 mA cm$^{-2}$, much higher than other as-prepared Ni-Ni$_3$C/NC catalysts (0.83~2.94 mA cm$^{-2}$) (Figure S7, ESI†), indicating a large surface area, fast electron transfer rate and favourable HER kinetics. Based on electrochemical double-layer capacitance ($C_{dl}$) measurements by cyclic voltammetry (CV) at different scan rates (Figures S8–S10, ESI†), the effective electrochemically active surface area (ECSA) can be studied as well. The ECSA of Ni-Ni$_3$C/NC-500 is 1990 cm$^2$, much larger than those of the other Ni-Ni$_3$C/NC catalysts (586~1162 cm$^2$). Importantly, from the ECSA-normalized LSV curves (Figure 3d), the Ni-Ni$_3$C/NC-500 catalyst still exhibits the highest activity. Moreover, the Ni-Ni$_3$C/NC-500 electrode has such excellent HER activity comparable to those of as-reported Ni-based materials (Figure 3e) and composites and various representative catalysts (Table S2, ESI†). Thus, the Ni-Ni$_3$C/NC-500 electrode is a catalyst with the best HER activity in alkaline solutions.

The electrochemical impedance spectra (EIS) (Figure 3f) confirms that Ni-Ni$_3$C/NC-500 has a smaller reaction resistance for HER due to its lowest charge transfer resistance (Rct = 4.4 Ω) compared with other samples, which is ascribed to the multi-heterostructures of Ni and Ni$_3$C and carbon coating to adjust the electronic structure and enhance the electron transfers. The Nyquist plots of Ni-Ni$_3$C/NC-500 were also measured at different potentials. As shown in Figure S11 (ESI†), the Rct value obviously decreases with the increase of the overpotentials, suggesting that under high overpotential, the electron transfer process of HER at the catalyst surface is accelerated. The electrochemical stability of Ni-Ni$_3$C/NC-500 was also measured using a long-term cyclic voltammetry test and time-dependent current density curves, as shown in Figure 4g,h. After 2000 and 5000 cycling tests, the polarization curve of Ni-Ni$_3$C/NC-500 shows no obvious potential decay. In addition, Ni-Ni$_3$C/NC-500 retains a stable current density over 100 h under a −0.2 V overpotential. Its stability is better than the other samples (Figure S12, ESI†), which should be related with its high-density heterostructure to maintain structural integrity. Various post-mortem characterizations, such as SEM, TEM, and XPS, reveal no evidence for the structure and phase changes of the Ni-Ni$_3$C/NC-500 after the HER durability test, as shown in Figures S13 and S14, which further proves the sample's superior electrochemical stability for long-term electrochemical processes in an alkaline electrolyte. Compared with other Ni-Ni$_3$C/NC samples, Ni-Ni$_3$C/NC-500 exhibits unceasing stability and structural robustness for HER in an alkaline solution. Meanwhile, the thermal stability of Ni-Ni$_3$C/NC-500 was also investigated by thermo-gravimetry. As shown in Figure S15, Ni-Ni$_3$C/NC was relatively stable in the temperature range of 100~800 °C, also meaning that few impurities remained.

### 2.3. Electrochemical OER and OWS of Ni-Ni$_3$C/NC

Then, the OER activity of Ni-Ni$_3$C/NCs is also investigated and recorded after 20 CV cycles in a 1 M KOH solution. As shown in Figure 4a, Ni-Ni$_3$C/NC-500 shows a very small onset overpotential of 267 mV for the OER process at 10 mA cm$^{-2}$, smaller than Ni-Ni$_3$C/NC-400 (341 mV), Ni-Ni$_3$C/NC-450 (322 mV), Ni-Ni$_3$C/NC-550 (323 mV), and Ni-Ni$_3$C/NC-650 (370 mV). The peaks located at 1.35~1.40 V are due to the transform of Ni$^{2+}$ to Ni$^{3+}$ [54]. A similar trend is also observed when the current density is increased to 100 mA cm$^{-2}$ (Figure 4b). These potentiometric responses are consistent with the LSV results (Figure 4a), which reflects that Ni-Ni$_3$C/NC-550 possesses excellent mass transport properties and a lower activation barrier. It is noteworthy that the OER catalytic performance of Ni-Ni$_3$C/NC is superior to all the Ni$_3$C-based electrocatalysts reported so far and is comparable to the most efficient nonprecious metal-based OER electrodes (Figure 4c and Table S3, ESI†). Meanwhile, Ni-Ni$_3$C/NC-500 exhibits the smallest Tafel slope of 81.99 mV dec$^{-1}$ among the samples obtained by us (Figure 4d), indicating its most rapid OER reaction kinetics. To gain further insight, OER reaction kinetics and EIS measurements were carried out, as shown in Figure 5e. The Nyquist plots disclose that

the interface charge transfer resistance of Ni-Ni$_3$C/NC-500 is the lowest, suggesting that Ni-Ni$_3$C/NC-500 owns the fastest charge transfer process during the OER process among all the samples investigated herein. Moreover, the chronopotentiometry (CP) measurement was performed to further investigate the stability. Ni-Ni$_3$C/NC-500 retains a stable over potential over 25 h of continuous operation at a current density of 25 mA cm$^{-2}$ with negligible change (Figure 5f). The potential retention rate from the initial time period of the stability test to the final time period is 105.3%. All the above results clearly illustrate that Ni-Ni$_3$C/NC-500 shows significantly enhanced electrocatalytic water oxidation in comparison with other Ni-Ni$_3$C/NC catalysts because of its sufficient heterostructure for interfacial electronic rearrangement and carbon coating.
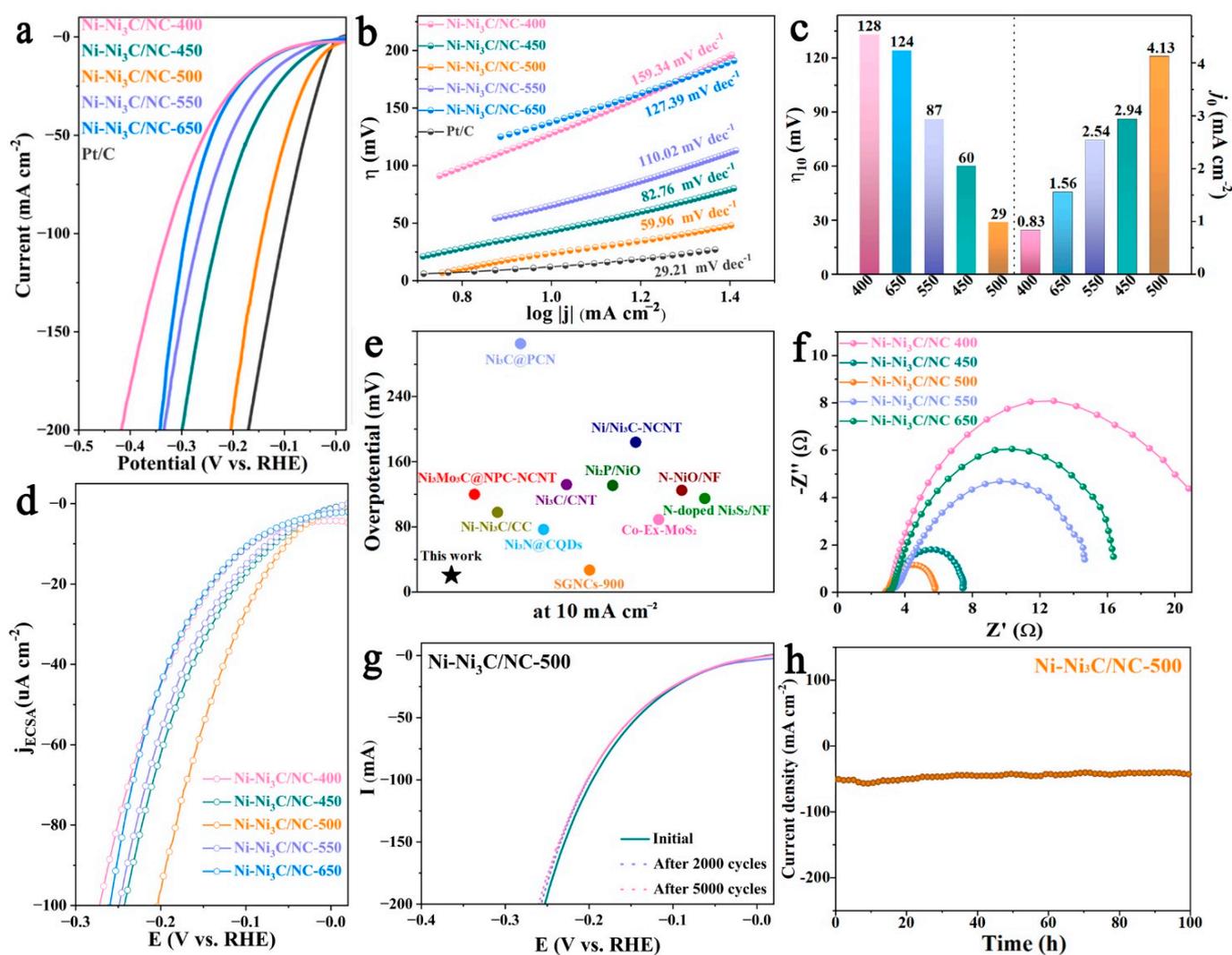


**Figure 3.** Electrochemical Property of Ni-Ni$_3$C/NC for HER. (**a**) Polarization curves of various Ni-Ni$_3$C/NC and Pt/C in 1.0 M KOH. (**b**) Tafel plots obtained from the polarization curves in (**a**). (**c**) Overpotentials at 10 mA cm$^{-2}$ (left) and exchange current densities (right). (**d**) ECSA-normalized LSV curves of various Ni-Ni$_3$C/NC. (**e**) The comparison of HER overpotentials at 10 mA cm$^{-2}$ for different catalysts. (**f**) The EIS plots of Ni-Ni$_3$C/NC measured at an overpotential of 150 mV (**g**) Polarization curves before and after 2000 and 5000 CV cycles of Ni-Ni$_3$C/NC-500. (**h**) A long-term current stability measurement of Ni-Ni$_3$C/NC-500 at a −0.2 V overpotential for 100 h.

In view of the excellent activity and durability of Ni-Ni$_3$C/NC heterostructures toward both OER and HER in an alkaline medium, the OWS performance was also evaluated in a two-electrode configuration (Figure S16, ESI†) employing Ni-Ni$_3$C/NC as the bifunctional

catalyst by LSV (Figure 4g,h). The Ni-Ni$_3$C/NC-500 catalyst shows that only 1.55 V and 1.26 V are required to achieve 10 mA cm$^{-2}$ and 1 mA cm$^{-2}$ water splitting current density in a two-electrode configuration. Their corresponding electricity-to-hydrogen efficiencies are 79–98% with respect to the lower heating value of hydrogen (237.18 kJ per mol produced H$_2$ or 1.229 V), whereas current commercial electrolysers operate at an efficiency between 60 to 73% [55]. Ni-Ni$_3$C/NC-500 retains a stable overpotential (~1.82 V) without compensation resistance iR over 25 h of continuous operation at a current density of 25 mA cm$^{-2}$ (Figure 4i). The potential retention rate of the stability test is as high as 99.7%, which confirms the sample's good stability in water electrolysis. In its OWS process, the volume-time curves (Figure S17, ESI†) reveal a volume ratio of 2.11:1 for the collected H$_2$ and O$_2$, which approaches the theoretical 2:1 ratio for water electrolysis. Based on the measured gases ratio, the faradic efficiency is estimated to be nearly 100%. These results undoubtedly demonstrate the importance of constructing heterostructures and the potentiality of Ni-Ni$_3$C/NC serves as a candidate catalyst for alkaline OWS.
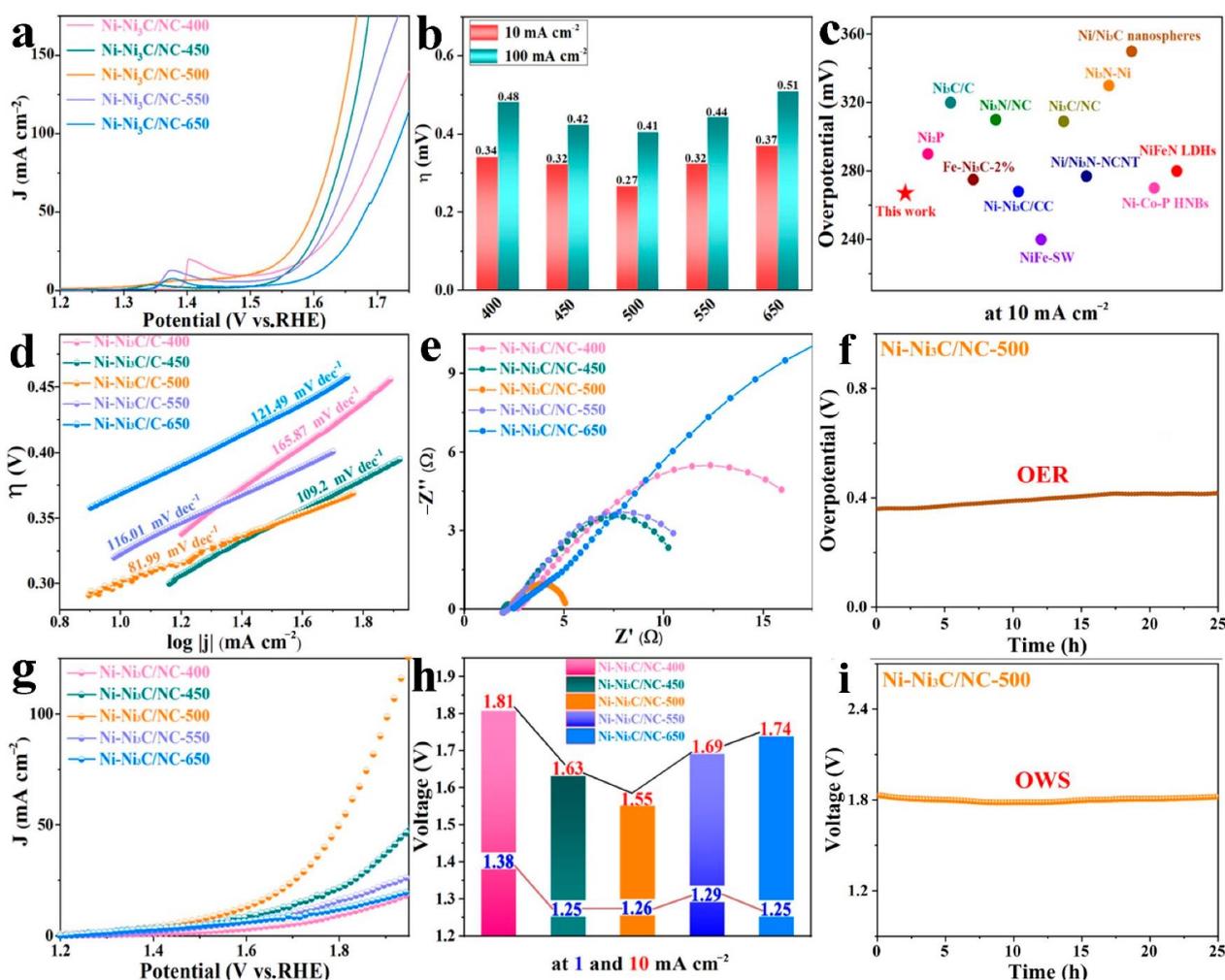


**Figure 4.** Electrochemical Properties of Ni-Ni$_3$C/NC for OER and OWS. (**a**) Polarization curves, (**b**) overpotential plots at 10 mA cm$^{-2}$ and 100 mA cm$^{-2}$, (**c**) The comparison of OER overpotentials at 10 mA cm$^{-2}$ for different catalysts. (**d**) Tafel slopes, (**e**) The EIS plots of Ni-Ni$_3$C/NC measured at an overpotential of 300 mV. (**f**) The long-term stability measurement of Ni-Ni$_3$C/NC-500 at a current density of 25 mA cm$^{-2}$ for 25 h. (**g,h**) The overall water splitting bi-functional activities were measured on Ni-Ni$_3$C/NC in a two-electrode configuration. The comparison of the cell voltage at 1 and 10 mA cm$^{-2}$ for Ni-Ni$_3$C/NC. (**i**) Time-dependent current density curve of Ni-Ni$_3$C/NC in 1 m KOH for 25 h without iR compensation.

*2.4. Interfacial Electronic Rearrangement and the Heterostructure's Synergistic Catalysis for HER and OER*

To further reveal the relationship of HER activity of the catalysts with the phase structure and heterojunction interface, we used DFT to calculate the optimized structures and free-energy diagrams for HER on Ni (111), $Ni_3C$ (113), and Ni (111)/$Ni_3C$ (113) catalysts (the structures are shown in Figure S18, ESI†). As shown in Figure 5a, an obvious charge rearrangement is observed around the Ni (111)/$Ni_3C$ (113) interface and a large number of electrons are transferred from $Ni_3C$ to metal Ni in the heterostructure, which means that metal Ni can provide electrons for hydrogen reduction. This result also agrees with the XPS peak shift in Figure 2. In the HER process, it has been well accepted that $H_2O$ dissociation to form adsorbed H* and OH* is the key step to evaluate overall catalytic activity [56,57] and, therefore, $H_2O$ dissociation free energies ($\Delta G_{diss}$) on the surfaces of Ni (111), $Ni_3C$ (113), and Ni (111)/$Ni_3C$ (113) are calculated. As shown in Figure 5b, it is concluded that $H_2O$ dissociation on Ni (111) and $Ni_3C$ (113) are endothermic processes with the $\Delta G_{diss}$ values of 0.37 and 2.89 eV, respectively. In contrast, the $H_2O$ dissociation on Ni (111)/$Ni_3C$ (113) heterostructures is an exothermic process with the $\Delta G_{diss}$ value of $-0.10$ eV. Therefore, the Ni (111)/$Ni_3C$ (113) heterostructure shows much better HER activity than Ni (111) or $Ni_3C$ (113) under alkaline conditions and performs as the active site for $H_2O$ dissociation. Compared with the optimized $H_2O$ molecular structures on Ni (111), $Ni_3C$ (113), and Ni (111)/$Ni_3C$ (113) (Figure 5c), it is found that for metal Ni (111) both the two hydrogen atoms of $H_2O$ are close to the metal Ni atom because of its empty d orbitals capable of binding H atoms, and for the $Ni_3C$ (113) oxygen atom of $H_2O$ lurching to the $Ni^{2+}$ atom. They are different from the Ni (111)/$Ni_3C$ (113) heterostructure, in which a hydrogen atom and oxygen atom in $-OH$ of $H_2O$ bound to the metal Ni atom and $Ni^{2+}$ atom in the heterostructure, respectively. Undoubtedly, the paired active sites in the heterostructure should have a stronger ability for cleaving HO-H bonds and weaker interaction of Ni-H. In this way, the multi-heterointerface will accelerate the subsequent generation of $H_2$.

To experimentally understand the Ni-$Ni_3C$/NC heterostructure electrodes during the HER and OER process, we used in-situ Raman spectroscopy to study it, as shown in Figure S19 (ESI†). The as-prepared Ni-$Ni_3C$/NC-500 sample, Hg/HgO, and Pt wires were used as working electrode, reference electrode, and counter electrode in the 1.0 M KOH electrolyte, respectively. As shown in Figure 5d, the in-situ Raman spectra of the Ni-$Ni_3C$/NC-500 electrode were collected at stepped potential values from $-0.15$ V to $+0.5$ V. The results show two gradually stronger characteristic peaks (486 and 542 cm$^{-1}$) of $Ni^{3+}$-OH$^{-}$ matched well with the spectral features of $\gamma$-NiOOH where the average oxidation state of Ni is +3.3 to 3.7 [58,59], a characteristic peak (1600 cm$^{-1}$) of Ni-H band and a vibrational peak (1634 cm$^{-1}$) of $-OH$ bending mode in $H_2O$ in HER and/or OER processes [60,61]. The gradually increasing signal of $-OH$ bending mode in $H_2O$ during HER is also detected in its in-situ FT-IR spectra, as shown in 5e. All the above signals of HER agree with the DFT calculation results in Figure 5c that the hydrogen atom and the oxygen atom in $-OH$ of $H_2O$ bound to the metal Ni atom and $Ni^{2+}$ atom in the Ni-$Ni_3C$ heterostructure, which resulted in the strengthened signal of the $-OH$ bending mode. Similarly, in the OER process, the hydrogen atom and the oxygen atom of OH$^{-}$ bound to the metal Ni atom and $Ni^{3+}$ (transformed from $Ni^{2+}$, which agrees with the LSV results in Figure 4a) in the Ni-$Ni_3C$ heterostructure. These effects undoubtedly elevated the water adsorption energy and lower $-OH$ or OH$^{-}$ anion adsorption energy, while leading to sufficient water adsorption and eliminating the $-OH$ or OH$^{-}$ poisoning effect attributed to a loss of the catalytically active site. The presence of $Ni_3C$ has the function to inhibit Ni self-oxidation and promote water dissociation into $H_2$ in the HER process by the formed $OH_{ad}$-$Ni^{2+}$ and $H_{ad}$-$Ni^0$ species, whereas OH$^{-}_{ad}$-$Ni^{3+}$ and $H_{ad}$-$Ni^0$ were created during the OER. Based on the above chemical state analysis from the in-situ Raman and FT-IR data, most importantly, the active surface species emerging at different potentials, and the overall working mechanism and active surface layers can be summarized (Figure 5f). The results

show that Ni and $Ni^{2+}$ species contribute equally to catalytic activity at different applied overpotentials, forming a synergistic effect beneficial for both the HER and OER reaction and resulting in the most effective bi-functional Ni-based heterostructure electrocatalysts to date.
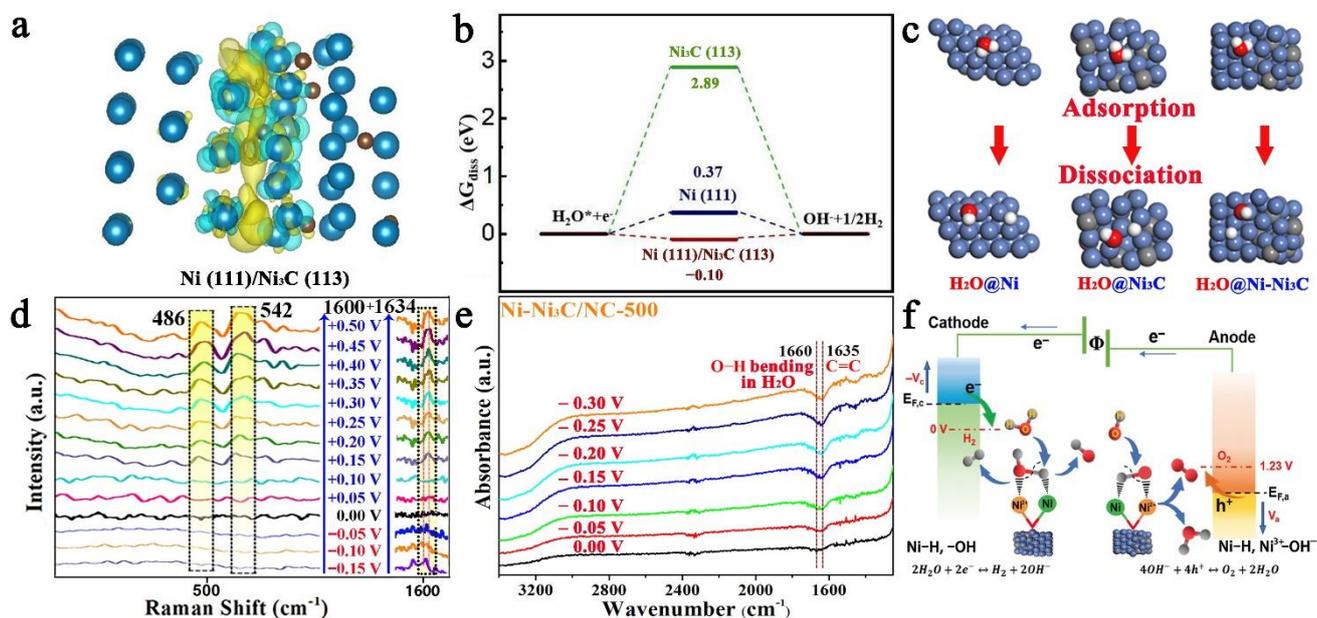


**Figure 5.** Interfacial electronic rearrangement and synergistic catalysis for alkaline water splitting. (**a**) Charge density difference map of Ni (111)/$Ni_3C$ (113) with an iso-surface value of 0.03 e Å$^{-3}$. (**b**) and (**c**) Gibbs free energy diagrams and the adsorption-dissociation of $H_2O$ on Ni (111), $Ni_3C$ (113), and Ni (111)/$Ni_3C$ (113) in an alkaline solution. Red and white balls represent oxygen and hydrogen atoms, respectively. (**d,e**) In-situ Raman spectrum and FT-IR spectrum measurements of Ni-$Ni_3C$/NC-500 under different electrochemical potentials. (**f**) Schematic representation of the electrocatalytic OWS in alkaline media. −OH and Ni-H are the formed surface adsorbed intermediates during the HER process, whereas Ni-H and $Ni^{3+}$-OH$^-$ are the observed surface intermediates during the OER process. The heterostructure electrocatalyst reduces the required driving energy and provides paired synergistically catalytic sites, and thus realizes a highly versatile energy conversion efficiency.

## 3. Materials and Methods

### 3.1. Materials

Nickel chloride ($NiCl_2 \cdot 6H_2O$, 98.5%), Isopropyl alcohol ($C_3H_8O$, 99.9%), Nitrilotriacetic acid ($N(CH_2COOH)_3$, 95%), sodium chloride (NaCl, 99.8%), sodium hydroxide (NaOH, 96%), ethanol (EtOH, 99.7%), and potassium hydroxide (KOH, 95%) were purchased from Sinopharm Chemical Reagent Co., Ltd, Shanghai, China. All chemical reagents were of analytical grade and used without further purification.

### 3.2. Synthesis of Ni-NTA Nanorods

In total, 0.35 g $NiCl_2 \cdot 6H_2O$ was added into 10 mL water and stirred until it was completely dissolved. Then, 0.2 g NTA and 20 mL isopropanol (IPA) were added into the solution and transferred to a 50 mL Teflon-lined stainless-steel autoclave. It was placed in an oven and maintained at 180 °C for 6 h. After the reaction, the product was poured into a centrifuge tube and centrifuged. The collected sample was then washed with distilled water and an ethanol solution several times and dried at 60 °C for 12 h.

### 3.3. Synthesis of Ni-Ni₃C/NC Porous Nanorods

The as-prepared Ni-NTA precursor was calcined in a Quartz tube furnace at different temperatures (400~650 °C) for 2 h in an argon atmosphere and collected.

### 3.4. Characterization

The X-ray powder diffraction (XRD, Bruker, Karlsruhe, Germany) test used a Cu-Kα radiation source with a wavelength of λ = 0.15405 nm. The Voltage and current in the process of testing were 40 kV and 150 mA, respectively. The scanning speed was $10°\ s^{-1}$ and the scanning area was from 20° to 80°. The field emission scanning electron microscopy (FE-SEM) images and energy dispersive X-ray spectrum (EDS) were taken on a SU8000 cold emission field scanning electron microanalyzer (Hitachi, Tokyo, Japan). Transmission electron microscopy (TEM), high-resolution transmission electron microscopy (HRTEM, FEI, Hillsboro, OR, USA), and scanning transmission electron microscopy with an energy dispersive X-ray (STEM-EDX) experiments were performed on a FEI Talos F200X G2 transmission electron microscope with a field emission gun operated at 200 kV. Fourier transform infrared (FTIR, Thermo Fisher Scientific, Waltham, MA, USA) spectra of the products were recorded on a Perkin-Elmer 580B IR spectrophotometer using the KBr pellet technique. $N_2$ adsorption/desorption examinations were conducted with a Micromeritics TriStar 3020 to characterize the Brunauer-Emmett-Teller (BET, Micromeritics, Atlanta, GA, USA) ratio of the sample. The test temperature was $-196.15\,°C$ (liquid nitrogen temperature), and the samples were heated at 120 °C for 2 h before the test. Raman spectra were taken using a Raman spectrometer (LABRAM HR800, HORIBA Jobin Yvon, Paris, France) with a 325 nm laser excitation. The samples were dispersed in ethanol for 30 min. X-ray photoelectron spectroscopy (XPS, (Kratos, Stretford, UK) was used to characterize the atomic composition content and the chemical valence state, which was equipped with an excitation source of 1486.6 eV of A1Kα target. The Operando ATR-IR measurement, the attenuated total reflectance surface enhanced infrared absorption spectroscopy (ATR-SEIRAS) experiments were taken with a Nicolet iS50 FT-IR spectrometer equipped with an MCT detector and PIKE VeeMAX III variable angle ATR sampling accessory. The spectral resolution was set to 4 $cm^{-1}$ and 64 interferograms were co-added for each spectrum. The spectra are given in absorption units defined as A = $-\log(R/R_0)$, where R and $R_0$ represent the reflected IR intensities corresponding to the sample and reference-single beam spectrum, respectively. A 60° Si face-angled crystal was used as reflection element. The angle of incidence was set as ca. 70°. In-situ Raman spectroscopic measurements were performed at room temperature using a HORIBA Lab Ram (HORIBA Jobin Yvon, Paris, France) spectrometer with a 785 nm excitation wavelength at 0.5 mW between 200 and 2500 $cm^{-1}$. To avoid laser-induced deintercalation and photochemistry, the laser power was kept below 0.5 MW and a laser spot size of 1 mm (Olympus LMPlanFl 50*, NA 0.50). A charge-coupled device was used to detect the signal after analyzing the signal via a monochromator. The spectrometer was calibrated in frequency using a HOPG crystal. A thermogravimetric analysis (TGA) experiment was carried out with a Perkin-Elmer TGA-7 thermogravimetric analyzer (PerkinElmer, Waltham, MA, USA) at a heating rate of $5\,°C·min^{-1}$ from 60 °C to 800 °C under nitrogen atmospheres.

### 3.5. Electrochemical Measurement

Electrochemical characterizations of these as-prepared catalysts were conducted on a CHI 660E electrochemical station using a three-electrode configuration. A Pt net was used as the counter electrode, a Hg/HgO electrode was used as the reference electrode, and the as-prepared catalyst was used as the working electrode. The stable polarization curve of each catalyst was recorded at a scan rate of 5 mV $s^{-1}$ with iR compensation after running at least 100 cyclic voltammetry (CV) cycles for activation and stabilization. An Hg/HgO electrode and graphite rod were used as the reference electrode and counter electrode, whereas various samples served as the working electrode. The potential ($E_{Hg/HgO}$) was calibrated to the reversible hydrogen electrode (RHE) using the equation:

$$E_{RHE} = E_{Hg/HgO} + 0.098 + 0.059 \times pH$$

and the overpotential ($\eta$) was calculated by:

$$\eta(V) = E_{RHE} - 1.23 \text{ V}$$

The Tafel slope (b) was calculated by:

$$\eta = a + b \log (j)$$

in which j is the current density. Electrochemical impedance spectroscopy (EIS) was performed from 100 kHz to 0.01 Hz. To evaluate the electrochemically active surface area (ECSA) of each catalyst, CV cycling was performed in the potential range from 0.724 to 0.824 V vs. RHE with scan rates ranging from 20 to 140 mV s$^{-1}$. By plotting the capacitive current at 0.78 V vs. RHE against the scan rates, the double-layer capacitance ($C_{dl}$) was obtained as half of the corresponding slope, and then the ECSA was derived from the equation:

$$ECSA = C_{dl}/C_s$$

in which $C_s$ is the specific capacitance for a flat surface (40 $\mu$F cm$^{-2}$).

## 4. Conclusions

In summary, we tackled the challenge by tuning surface electronic structures synergistically with interfacial chemistry and crystal facet engineering, and successfully designing and synthesizing electrocatalysts with a carbon-encapsulated Ni (111)/Ni$_3$C (113) heterojunction, demonstrating superior HER activities and good stabilities with a small overpotential of $-29$ mV at 10 mA/cm$^2$, and a low Tafel slope of 59.96 mV/dec in alkaline surroundings, approximating a commercial Pt/C catalyst and outperforming other reported Ni-based catalysts. In OWS, the material system operates at 1.55 V and 1.26 V to reach 10 and 1 mA cm$^{-2}$ in two-electrode measurements, corresponding to 79% and 98% electricity-to-fuel conversion efficiency with respect to the lower heating value of hydrogen. Theoretical calculation and experiments verified that the heterojunction of Ni (111)/Ni$_3$C (113) can effectively regulate its electronic structure for lowering the Gibbs free energy of H$_2$O dissociation and form a synergistic effect beneficial for both HER and OER reactions. Additionally, the carbon shell as an effective protection layer holds the Ni/Ni$_3$C core active site and prevents oxidation by dissolved oxygen or oxygen generated from the counter electrodes. The system can be applied as a low-cost, efficient, and durable bi-functional catalyst, which bears promises for integration into renewable technologies, such as fuel formation from wind- or solar-based electricity in alkaline for sustainable production of hydrogen.

**Supplementary Materials:** The supporting information can be downloaded at: https://www.mdpi.com/article/10.3390/catal12111367/s1. Figure S1: Microstructure and composition characterizations of the as-obtained Ni-NTA precursor. (a) FT-IR spectrum; (b) SEM images; (c,d) TEM images. Figure S2: SEM images of (a) Ni-Ni$_3$C/NC-400, (b) Ni-Ni$_3$C/NC-450, (c) Ni-Ni$_3$C/NC-550, and (d) Ni-Ni$_3$C/NC-650. Figure S3: TEM images of the (a) Ni-Ni$_3$C/NC-400, (b) Ni-Ni$_3$C/NC-450, (c) Ni-Ni$_3$C/NC-550 and (d) Ni-Ni$_3$C/NC-650. Figure S4: (a–c) N$_2$ adsorption-desorption isotherms and (d–f) pore-size distribution curves of the Ni-Ni$_3$C/NC-450, Ni-Ni$_3$C/NC-500 and Ni-Ni$_3$C/NC-550. Figure S5: XPS spectra of Ni-Ni$_3$C/NC-450, Ni-Ni$_3$C/NC-500 and Ni-Ni$_3$C/NC-550: (a–c) Full XPS spectra; (d-f) Their entire Ni 2p spectra. Figure S6: The equipment picture of alkaline HER test in 1 M KOH solution. Figure S7: Exchange current densities (j$_0$) of Ni-Ni$_3$C/NC-400, Ni-Ni$_3$C/NC-450, Ni-Ni$_3$C/NC-500, Ni-Ni$_3$C/NC-550, Ni-Ni$_3$C/NC-650 and Pt/C, are determined by using extrapolation method. Figure S8: The extraction of the C$_{dl}$ and CV with different rates (20~120 mV/S) for Ni-Ni$_3$C/NC-500. Figure S9: CV curves for calculation of double-layer capacitance. CV curves of Ni-Ni$_3$C/NC-400, Ni-Ni$_3$C/NC-450, Ni-Ni$_3$C/NC-550, Ni-Ni$_3$C/NC-650 at scan rates ranging from 20 mV S$^{-1}$. Figure S10: The capacitive current densities measured at 0.25 V vs. RHE with different scan rates. Figure S11: The corresponding Nyquist plots of Ni-Ni$_3$C/NC-500 at various voltages in 1M KOH. Figure S12: Polarization curves before and after 2000 CV cycles

and the long-term stability measurements of Ni-Ni$_3$C/NC-400, Ni-Ni$_3$C/NC-450, Ni-Ni$_3$C/NC-550 and Ni-Ni$_3$C/NC-650 at 25 mA cm$^{-1}$ constant current density. Figure S13: (a, b) SEM micrograph, (c, d) TEM micrograph of Ni-Ni$_3$C/NC-500 after a 100 h HER measurement. Figure S14: XPS spectra of Ni-Ni$_3$C/NC-500 after a 10 h long-term HER test. Figure S15: Thermogravimetric analysis (TGA) curve of Ni-Ni$_3$C/NC-500. Figure S16: The equipment picture of alkaline OWS test in 1 M KOH solution. Figure S17: The volumes of H$_2$ and O$_2$ as a function of time in the electrocatalytic overall water splitting. Figure S18: Side (top) and top (bottom) view of three surfaces, including Ni (111), Ni$_3$C (113) and Ni (111)/Ni$_3$C (113). Figure S19: The equipment picture of in-situ electrochemical Raman spectrum. Table S1: N$_2$ adsorption-desorption isotherms and pore-size distribution curves of the Ni-Ni$_3$C/NC-450, Ni-Ni$_3$C/NC-500 and Ni-Ni$_3$C/NC-550. Table S2: Comparison of catalytic parameters of Ni-Ni$_3$C/NC-500 and other Ni-based HER composite-catalysts in alkaline media. Table S3: Comparison of catalytic parameters of Ni-Ni$_3$C/NC-500 and other Ni-based OER composite-catalysts in alkaline media. [62–70].

**Author Contributions:** P.G., X.L., and D.J. conceived of the idea, and designed and performed the experiments as well as the data analysis. W.W. and Z.P. contributed to the TEM and EELS measurements as well as the EELS analysis. P.D. and Y.W. conducted the SEM and EDX measurements. X.X. and M.X. analyzed and interpreted the HRTEM. P.G. and X.L. co-wrote the manuscript. G.J. and W.Y. performed the analysis, and P.G supervised and supported the work. All authors have read and agreed to the published version of the manuscript.

**Data Availability Statement:** Data are available on request.

**Conflicts of Interest:** The authors declare no conflict of interest.

# References

1. Zhang, B.; Qiu, C.; Wang, S.; Gao, H.; Yu, K.; Zhang, Z.; Ling, X.; Ou, W.; Su, C. Electrocatalytic water-splitting for the controllable and sustainable synthesis of deuterated chemicals. *Sci. Bull.* **2021**, *66*, 562–569. [CrossRef]
2. Gandía, L.M.; Oroz, R.; Ursúa, A.; Sanchis, P.; Diéguez, P.M. Renewable Hydrogen Production: Performance of an Alkaline Water Electrolyzer Working under Emulated Wind Conditions. *Energy Fuels* **2007**, *21*, 1699–1706. [CrossRef]
3. Zhu, S.; Wang, Z.; Huang, F.; Zhang, H.; Li, S. Hierarchical Cu(OH)$_2$@Ni$_2$(OH)$_2$CO$_3$ core/shell nanowire arrays in situ grown on three-dimensional copper foam for high-performance solid-state supercapacitors. *J. Mater. Chem. A* **2017**, *5*, 9960–9969. [CrossRef]
4. Dong, Z.; Lin, F.; Yao, Y.; Jiao, L. Crystalline Ni(OH)$_2$/Amorphous NiMoO$_x$ Mixed-Catalyst with Pt-Like Performance for Hydrogen Production. *Adv. Energy Mater.* **2019**, *9*, 1902703. [CrossRef]
5. Wu, Z.; Zou, Z.; Huang, J.; Gao, F. Fe-doped NiO mesoporous nanosheets array for highly efficient overall water splitting. *J. Catal.* **2018**, *358*, 243–252. [CrossRef]
6. Sun, Q.; Dong, Y.; Wang, Z.; Yin, S.; Zhao, C. Synergistic Nanotubular Copper-Doped Nickel Catalysts for Hydrogen Evolution Reactions. *Small* **2018**, *14*, e1704137. [CrossRef]
7. Wang, J.; Xie, Y.; Yao, Y.; Huang, X.; Willinger, M.; Shao, L. Ni/NiO nanoparticles on a phosphorous oxide/graphene hybrid for efficient electrocatalytic water splitting. *J. Mater. Chem. A* **2017**, *5*, 14758–14762. [CrossRef]
8. Zhang, J.; Wang, T.; Liu, P.; Liu, S.; Dong, R.; Zhuang, X.; Chen, M.; Feng, X. Engineering water dissociation sites in MoS$_2$ nanosheets for accelerated electrocatalytic hydrogen production. *Energy Environ. Sci.* **2016**, *9*, 2789–2793. [CrossRef]
9. Zhang, B.; Liu, J.; Wang, J.; Ruan, Y.; Ji, X.; Xu, K.; Chen, C.; Wan, H.; Miao, L.; Jiang, J. Interface engineering: The Ni(OH)$_2$/MoS$_2$ heterostructure for highly efficient alkaline hydrogen evolution. *Nano Energy* **2017**, *37*, 74–80. [CrossRef]
10. Lin, H.; Shi, Z.; He, S.; Yu, X.; Wang, S.; Gao, Q.; Tang, Y. Heteronanowires of MoC-Mo$_2$C as efficient electrocatalysts for hydrogen evolution reaction. *Chem. Sci.* **2016**, *7*, 3399–3405. [CrossRef]
11. Liao, L.; Wang, S.; Xiao, J.; Bian, X.; Zhang, Y.; Scanlon, M.D.; Hu, X.; Tang, Y.; Liu, B.; Girault, H.H. A nanoporous molybdenum carbide nanowire as an electrocatalyst for hydrogen evolution reaction. *Energy Environ. Sci.* **2014**, *7*, 387–392. [CrossRef]
12. Wang, C.; Jiang, J.; Ding, T.; Chen, G.; Xu, W.; Yang, Q. Monodisperse Ternary NiCoP Nanostructures as a Bifunctional Electrocatalyst for Both Hydrogen and Oxygen Evolution Reactions with Excellent Performance. *Adv. Mater. Interfaces* **2016**, *3*, 1500454. [CrossRef]

13. Stern, L.A.; Feng, L.; Song, F.; Hu, X. $Ni_2P$ as a Janus catalyst for water splitting: The oxygen evolution activity of $Ni_2P$ nanoparticles. *Energy Environ. Sci.* **2015**, *8*, 2347–2351. [CrossRef]

14. Wang, Z.L.; Xu, D.; Xu, J.J.; Zhang, X.B. Oxygen electrocatalysts in metal-air batteries: From aqueous to nonaqueous electrolytes. *Chem. Soc. Rev.* **2014**, *43*, 7746–7786. [CrossRef] [PubMed]

15. Xi, W.; Ren, Z.; Kong, L.; Wu, J.; Du, S.; Zhu, J.; Xue, Y.; Meng, H.; Fu, H. Dual-valence nickel nanosheets covered with thin carbon as bifunctional electrocatalysts for full water splitting. *J. Mater. Chem. A* **2016**, *4*, 7297–7304. [CrossRef]

16. Conway, B.E.; Jerkiewicz, G. Relation of energies and coverages of underpotential and overpotential deposited H at Pt and other metals to the 'volcano curve' for cathodic $H_2$ evolution kinetics. *Electrochim. Acta* **2000**, *45*, 4075–4083. [CrossRef]

17. Xiao, P.; Sk, M.A.; Thia, L.; Ge, X.; Lim, R.J.; Wang, J.Y.; Lim, K.H.; Wang, X. Molybdenum phosphide as an efficient electrocatalyst for the hydrogen evolution reaction. *Energy Environ. Sci.* **2014**, *7*, 2624–2629. [CrossRef]

18. Chen, Y.; Xu, S.; Li, Y.; Jacob, R.J.; Kuang, Y.; Liu, B.; Wang, Y.; Pastel, G.; Salamanca-Riba, L.G.; Zachariah, M.R.; et al. $FeS_2$ Nanoparticles Embedded in Reduced Graphene Oxide toward Robust, High-Performance Electrocatalysts. *Adv. Energy Mater.* **2017**, *7*, 1700482. [CrossRef]

19. Zhou, G.; Li, M.; Li, Y.; Dong, H.; Sun, D.; Liu, X.; Xu, L.; Tian, Z.; Tang, Y. Regulating the Electronic Structure of CoP Nanosheets by O Incorporation for High-Efficiency Electrochemical Overall Water Splitting. *Adv. Funct. Mater.* **2019**, *30*, 1905252. [CrossRef]

20. Lei, C.; Wang, Y.; Hou, Y.; Liu, P.; Yang, J.; Zhang, T.; Zhuang, X.; Chen, M.; Yang, B.; Lei, L.; et al. Efficient alkaline hydrogen evolution on atomically dispersed $Ni-N_x$ Species anchored porous carbon with embedded Ni nanoparticles by accelerating water dissociation kinetics. *Energy Environ. Sci.* **2019**, *12*, 149–156. [CrossRef]

21. Jain, A.; Castelli, I.E.; Hautier, G.; Bailey, D.H.; Jacobsen, K.W. Performance of genetic algorithms in search for water splitting perovskites. *J. Mater. Sci.* **2013**, *48*, 6519–6534. [CrossRef]

22. Sun, H.; Li, L.; Humayun, M.; Zhang, H.; Bo, Y.; Ao, X.; Xu, X.; Chen, K.; Ostrikov, K.; Huo, K.; et al. Achieving highly efficient pH-universal hydrogen evolution by superhydrophilic amorphous/crystalline $Rh(OH)_3$/NiTe coaxial nanorod array electrode. *Appl. Catal. B Environ.* **2022**, *305*, 121088. [CrossRef]

23. Danilovic, N.; Subbaraman, R.; Chang, K.C.; Chang, S.H.; Kang, Y.; Snyder, J.; Paulikas, A.P.; Strmcnik, D.; Kim, Y.T.; Myers, D.; et al. Using surface segregation to design stable Ru-Ir oxides for the oxygen evolution reaction in acidic environments. *Angew. Chem. Int. Ed.* **2014**, *53*, 14016–14021. [CrossRef] [PubMed]

24. Gong, M.; Zhou, W.; Tsai, M.C.; Zhou, J.; Guan, M.; Lin, M.C.; Zhang, B.; Hu, Y.; Wang, D.Y.; Yang, J.; et al. Nanoscale nickel oxide/nickel heterostructures for active hydrogen evolution electrocatalysis. *Nat. Commun.* **2014**, *5*, 4695. [CrossRef]

25. Gong, M.; Zhou, W.; Kenney, M.J.; Kapusta, R.; Cowley, S.; Wu, Y.; Lu, B.; Lin, M.C.; Wang, D.Y.; Yang, J.; et al. Blending $Cr_2O_3$ into a NiO-Ni electrocatalyst for sustained water splitting. *Angew. Chem. Int. Ed.* **2015**, *54*, 11989–11993. [CrossRef]

26. Wang, P.; Qin, R.; Ji, P.; Pu, Z.; Zhu, J.; Lin, C.; Zhao, Y.; Tang, H.; Li, W.; Mu, S. Synergistic Coupling of Ni Nanoparticles with $Ni_3$C Nanosheets for Highly Efficient Overall Water Splitting. *Small* **2020**, *16*, e2001642. [CrossRef]

27. Dong, T.; Zhang, X.; Cao, Y.; Chen, H.S.; Yang, P. $Ni/Ni_3C$ core-shell nanoparticles encapsulated in N-doped bamboo-like carbon nanotubes towards efficient overall water splitting. *Inorg. Chem. Front.* **2019**, *6*, 1073–1080. [CrossRef]

28. Xiong, W.; Guo, Q.; Guo, Z.; Li, H.; Zhao, R.; Chen, Q.; Liu, Z.; Wang, X. Atomic layer deposition of nickel carbide for supercapacitors and electrocatalytic hydrogen evolution. *J. Mater. Chem. A* **2018**, *6*, 4297–4304. [CrossRef]

29. Wang, H.; Cao, Y.; Zou, G.; Yi, Q.; Guo, J.; Gao, L. High-Performance Hydrogen Evolution Electrocatalyst Derived from $Ni_3C$ Nanoparticles Embedded in a Porous Carbon Network. *ACS Appl. Mater. Interfaces* **2017**, *9*, 60–64. [CrossRef]

30. Zhu, G.; Peng, Z.; Hu, Z.; Bian, J.; Ye, W.; Wu, T.; Chen, Y.; Gao, P. Abundant hot-spot construction between Ni/C nanotubes with enhanced localized surface plasmon resonance for Radar wave absorption. *Appl. Surf. Sci.* **2020**, *504*, 144592. [CrossRef]

31. Chhetri, K.; Muthurasu, A.; Dahal, B.; Kim, T.; Mukhiya, T.; Chae, S.H.; Ko, T.H.; Choi, Y.C.; Kim, H.Y. Engineering the abundant heterointerfaces of integrated bimetallic sulfide-coupled 2D MOF-derived mesoporous $CoS_2$ nanoarray hybrids for electrocatalytic water splitting. *Mater. Today Nano* **2022**, *17*, 100146. [CrossRef]

32. Chhetri, K.; Dahal, B.; Mukhiya, T.; Tiwari, A.P.; Muthurasu, A.; Kim, T.; Kim, H.; Kim, H.Y. Integrated hybrid of graphitic carbon-encapsulated $Cu_xO$ on multilayered mesoporous carbon from copper MOFs and polyaniline for asymmetric supercapacitor and oxygen reduction reactions. *Carbon* **2021**, *179*, 89–99. [CrossRef]

33. Torregrosa-Rivero, V.; Sánchez-Adsuar, M.S.; Illán-Gómez, M.J. Analyzing the role of copper in the soot oxidation performance of $BaMnO_3$-perovskite-based catalyst obtained by modified sol-gel synthesis. *Fuel* **2022**, *328*, 125258. [CrossRef]

34. Qiu, C.; Wang, S.; Zuo, J.; Zhang, B. Photocatalytic $CO_2$ Reduction Coupled with Alcohol Oxidation over Porous Carbon Nitride. *Catalysts* **2022**, *12*, 672. [CrossRef]

35. Abdullah, F.; Mohd Yusoff, A.R.; Wan Abu Bakar, W.A.; Ismail, R.; Syafiuddin, A. Preparation, characterization, and lead removal appraisal of zinc aluminate prepared at different calcination temperatures. *J. Chin. Chem. Soc.* **2018**, *65*, 1199–1209. [CrossRef]

36. Kandel, M.R.; Pan, U.N.; Paudel, D.R.; Dhakal, P.P.; Kim, N.H.; Lee, J.H. Hybridized bimetallic phosphides of Ni-Mo, Co-Mo, and Co-Ni in a single ultrathin-3D-nanosheets for efficient HER and OER in alkaline media. *Compos. Part B Eng.* **2022**, *239*, 109992. [CrossRef]

37. Yang, Y.; Sun, X.; Han, G.; Liu, X.; Zhang, X.; Sun, Y.; Zhang, M.; Cao, Z.; Sun, Y. Enhanced Electrocatalytic Hydrogen Oxidation on Ni/NiO/C Derived from a Nickel-Based Metal-Organic Framework. *Angew. Chem. Int. Ed.* **2019**, *58*, 10644–10649. [CrossRef]

38. Qin, Q.; Hao, J.; Zheng, W. $Ni/Ni_3C$ Core/Shell Hierarchical Nanospheres with Enhanced Electrocatalytic Activity for Water Oxidation. *ACS Appl. Mater. Interfaces* **2018**, *10*, 17827–17834. [CrossRef]

39. Ferrari, A.C.; Robertson, J. Resonant Raman spectroscopy of disordered, amorphous, and diamondlike carbon. *Phys. Rev. B* **2001**, *64*, 075414. [CrossRef]

40. Yan, B.; Liu, D.; Feng, X.; Shao, M.; Zhang, Y. Ru Nanoparticles Supported on Co-Embedded N-Doped Carbon Nanotubes as Efficient Electrocatalysts for Hydrogen Evolution in Basic Media. *Chem. Res. Chin. Univ.* **2020**, *36*, 425–430. [CrossRef]

41. Cui, X.; Chen, X.; Chen, S.; Jia, F.; Yang, S.; Lin, Z.; Shi, Z.; Deng, H. Dopamine adsorption precursor enables N-doped carbon sheathing of $MoS_2$ nanoflowers for all-around enhancement of supercapacitor performance. *J. Alloys Comp.* **2017**, *693*, 955–963. [CrossRef]

42. Cao, D.; Kang, W.; Huang, Z.; Li, H.; Yang, M.; Li, J.; Gao, Y.; Wang, Y.; Ma, P.; Sun, D. N-doped carbon matrix supported $Fe_3Ni_6S_8$ hierarchical architecture with excellent sodium storage capability and electrocatalytic properties. *Electrochim. Acta* **2019**, *325*, 134925. [CrossRef]

43. Shang, Y.; Ding, Y.; Zhang, P.; Wang, M.; Jia, Y.; Xu, Y.; Li, Y.; Fan, K.; Sun, L. Pyrrolic N or pyridinic N: The active center of N-doped carbon for $CO_2$ reduction. *Chin. J. Catal.* **2022**, *43*, 2405–2413. [CrossRef]

44. Zhao, D.; Sun, K.; Cheong, W.C.; Zheng, L.; Zhang, C.; Liu, S.; Cao, X.; Wu, K.; Pan, Y.; Zhuang, Z.; et al. Synergistically Interactive Pyridinic-N-MoP Sites: Identified Active Centers for Enhanced Hydrogen Evolution in Alkaline Solution. *Angew. Chem. Int. Ed.* **2020**, *59*, 8982–8990. [CrossRef]

45. Hall, D.S.; Bock, C.; MacDougall, B.; David, L.; Poirier, S. A Spectroscopic and Electrochemical Investigation of the Structure of $Ni(OH)_2$ Materials. *ECS Meet. Abst.* **2012**, *MA2012–02*, 2208. [CrossRef]

46. Faid, A.Y.; Barnett, A.O.; Seland, F.; Sunde, S. Ni/NiO nanosheets for alkaline hydrogen evolution reaction: In situ electrochemical-Raman study. *Electrochim. Acta* **2020**, *361*, 137040. [CrossRef]

47. Huang, J.; Li, Y.; Zhang, Y.; Rao, G.; Wu, C.; Hu, Y.; Wang, X.; Lu, R.; Li, Y.; Xiong, J. Identification of Key Reversible Intermediates in Self-Reconstructed Nickel-Based Hybrid Electrocatalysts for Oxygen Evolution. *Angew. Chem. Int. Ed.* **2019**, *58*, 17458–17464. [CrossRef]

48. Yu, X.; Zhao, J.; Zheng, L.R.; Tong, Y.; Zhang, M.; Xu, G.; Li, C.; Ma, J.; Shi, G. Hydrogen Evolution Reaction in Alkaline Media: Alpha- or Beta-Nickel Hydroxide on the Surface of Platinum? *ACS Energy Lett.* **2017**, *3*, 237–244. [CrossRef]

49. Patel, K.N.; Deshpande, M.P.; Gujarati, V.P.; Pandya, S.; Sathe, V.; Chaki, S.H. Structural and optical analysis of Fe doped NiO nanoparticles synthesized by chemical precipitation route. *Mater. Res. Bull.* **2018**, *106*, 187–196. [CrossRef]

50. Karishma; Tripathi, N.; Yanagida, M.; Nagataki, A.; Tripathi, A.; Sharma, V. Synthesis and characterization of Na-doped NiO nanocrystals. *Mater. Today Proc.* **2020**, *28*, 269–271.

51. Qiu, Z.; Ma, Y.; Edvinsson, T. In operando Raman investigation of Fe doping influence on catalytic NiO intermediates for enhanced overall water splitting. *Nano Energy* **2019**, *66*, 104118. [CrossRef]

52. Fichtner, C.; Laurich, C.; Bothe, E.; Lubitz, W. Spectroelectrochemical Characterization of the [NiFe] Hydrogenase of Desulfovibrio vulgaris Miyazaki F. *Biochemistry* **2006**, *45*, 9706–9716. [CrossRef] [PubMed]

53. Shinagawa, T.; Garcia-Esparza, A.T.; Takanabe, K. Insight on Tafel slopes from a microkinetic analysis of aqueous electrocatalysis for energy conversion. *Sci. Rep.* **2015**, *5*, 13801. [CrossRef] [PubMed]

54. Wang, J.; Li, K.; Zhong, H.X.; Xu, D.; Wang, Z.L.; Jiang, Z.; Wu, Z.J.; Zhang, X.B. Synergistic Effect between Metal-Nitrogen-Carbon Sheets and NiO Nanoparticles for Enhanced Electrochemical Water-Oxidation Performance. *Angew. Chem. Int. Ed.* **2015**, *54*, 10530–10534. [CrossRef]

55. Turner, J.A. Sustainable Hydrogen Production. *Science* **2004**, *305*, 972–974. [CrossRef]

56. Liu, X.; Jiao, Y.; Zheng, Y.; Davey, K.; Qiao, S.Z. A computational study on Pt and Ru dimers supported on graphene for the hydrogen evolution reaction: New insight into the alkaline mechanism. *J. Mater. Chem. A* **2019**, *7*, 3648–3654. [CrossRef]

57. Li, L.; Zhang, G.; Wang, B.; Yang, T.; Yang, S. Electrochemical formation of PtRu bimetallic nanoparticles for highly efficient and pH-universal hydrogen evolution reaction. *J. Mater. Chem. A* **2020**, *8*, 2090–2098. [CrossRef]

58. Yeo, B.S.; Bell, A.T. In Situ Raman Study of Nickel Oxide and Gold-Supported Nickel Oxide Catalysts for the Electrochemical Evolution of Oxygen. *J. Phys. Chem. C* **2012**, *116*, 8394–8400. [CrossRef]

59. Klaus, S.; Cai, Y.; Louie, M.W.; Trotochaud, L.; Bell, A.T. Effects of Fe Electrolyte Impurities on $Ni(OH)_2$/NiOOH Structure and Oxygen Evolution Activity. *J. Phys. Chem. C* **2015**, *119*, 7243–7254. [CrossRef]

60. Morrow, B.A.; Hardin, A.H. Raman spectra of some hydrogen sequestering agents chemisorbed on silica. *J. Phys. Chem.* **1979**, *83*, 3135–3141. [CrossRef]

61. Qiu, Z.; Tai, C.W.; Niklasson, G.A.; Edvinsson, T. Direct observation of active catalyst surface phases and the effect of dynamic self-optimization in NiFe-layered double hydroxides for alkaline water splitting. *Energy Environ. Sci.* **2019**, *12*, 572–581. [CrossRef]

62. Kresse, G.; Furthmüller, J. Efficient iterative schemes for ab initio total-energy calculations using a plane-wave basis set. *Phys. Rev. B* **1996**, *54*, 11169–11186. [CrossRef] [PubMed]

63. Kresse, G.; Joubert, D. From ultrasoft pseudopotentials to the projector augmented-wave method. *Phys. Rev. B* **1999**, *59*, 1758–1775. [CrossRef]

64. Perdew, J.P.; Burke, K.; Ernzerhof, M. Generalized Gradient Approximation Made Simple. *Phys. Rev. Lett.* **1996**, *77*, 3865–3868. [CrossRef] [PubMed]

65. Grimme, S. Density functional theory with London dispersion corrections. *WIREs Comput. Mol. Sci.* **2011**, *1*, 211–228. [CrossRef]

66. Steinmann, S.N.; Corminboeuf, C. A System-Dependent Density-Based Dispersion Correction. *J. Chem. Theory Comput.* **2010**, *6*, 1990–2001. [CrossRef]

67. Nørskov, J.K.; Bligaard, T.; Logadottir, A.; Kitchin, J.R.; Chen, J.G.; Pandelov, S.; Stimming, U. Trends in the Exchange Current for Hydrogen Evolution. *J. Electrochem. Soc.* **2005**, *152*, J23. [CrossRef]
68. Peterson, A.A.; Abild-Pedersen, F.; Studt, F.; Rossmeisl, J.; Nørskov, J.K. How copper catalyzes the electroreduction of carbon dioxide into hydrocarbon fuels. *Energy Environ. Sci.* **2010**, *3*, 1311–1315. [CrossRef]
69. Tsuboi, M.; Onishi, T.; Nakagawa, I.; Shimanouchi, T.; Mizushima, S.I. Assignments of the vibrational frequencies of glycine. *Spectrochim. Acta* **1958**, *12*, 253–261. [CrossRef]
70. Reddy, A.L.M.; Shaijumon, M.M.; Gowda, S.R.; Ajayan, P.M. Coaxial $MnO_2$/carbon nanotube array electrodes for high-performance lithium batteries. *Nano lett.* **2009**, *9*, 1002–1006. [CrossRef]